Motion and Stability of Cones in a Yield Stress Fluid

Fiacre Ahonguio, Laurent Jossic, and Albert Magnin
Université Grenoble Alpes, LRP, F-38000 Grenoble, France

CNRS, LRP, F-38000 Grenoble, France

DOI 10.1002/aic.14651
Published online October 29, 2014 in Wiley Online Library (wileyonlinelibrary.com)

This experimental study focuses on the creeping flow of a shear thinning yield stress fluid around conical obstacles. The flow has been analyzed in steady state and with adherence conditions. Firstly, the influences of the cone apex angle and of the Oldroyd number, that is the ratio between plastic and viscous effects, on the drag coefficient have been analyzed. Correlations have been proposed to model the evolution of this coefficient as a function of these two parameters. The analysis provides a new alternative for measuring the yield stress. Then, the kinematic fields around the cones have been analyzed. These fields enable to describe the rigid zones and the sheared zone developing around the lateral edge of the cones as a function of the cone apex angle. Moreover, the wall shear stresses estimated from the particle image velocimetry measurements have enabled to quantify the contribution of the lateral drag force in the drag force. © 2014 American Institute of Chemical Engineers *AIChE J*, 61: 709–717, 2015
Keywords: cone, drag, sheared zone, velocity profiles, yield stress fluid

Introduction

The dynamics of objects moving in media, especially in viscoplastic media, is extensively studied due to its numerous applications. As an illustration, objects are often sunk into some media to characterize their stiffness or hardness, their consistency, their structure, and so forth. This technique is used in fall tests using cones, footings or shallow penetrometers in geotechnics. The presence of the yield stress is also used in cosmetics, food processing and oil industries to ensure the keeping in suspension and the stability of objects with different shapes. The objects that have hitherto received the most interest in viscoplastic media are the sphere[1–20] and the cylinder.[21–24] However, some studies have paid attention on the flat plate[25–28] and on the disc.[29] All these experimental, theoretical and numerical studies aforementioned have enabled to characterize the flow morphology in the vicinity of the considered obstacle. They have in particular enabled to describe the shape and the extent of the rigid and sheared zones.

This study focuses on the creeping flow of a shear thinning yield stress fluid around adhesive (i.e. no-slip at the wall) conical obstacles in steady state. The upstream velocity field is uniform and the fluid flows along the cone's axis of symmetry. The experimental, numerical and theoretical data concerning this flow configuration are still fragmented. They mainly concern hardness tests performed by the fall cone tests. It is worth noting that in most of these tests the cones used are not completely embedded in the considered medium.

Correspondence concerning this article should be addressed to L. Jossic at laurent.jossic@grenoble-inp.fr.

Houlsby[30] and Houlsby and Wroth[31] have paid attention on the theoretical calculations of the force undergone by a rigid-plastic medium submitted to hardness tests with conical penetrometers. In their studies based on the method of characteristics, they analyzed the effects of the cone apex angle and of the roughness of the cones on the force. They estimated the force to be proportional to the cross section of the cones and to the load applied to the penetrometer. Noting N_c the cone bearing capacity factor, they observed a decrease of N_c with the cone apex angle in a homogeneous medium for a given roughness. Koumoto and Houlsby[32] have performed a similar analysis, both theoretically and experimentally, by taking into account the soil heave. They shown that in addition to the angle and roughness of the cone, the strain of the free surface of the medium can also influence the value of the bearing capacity factor N_{ch} estimated by considering the soil heave.

Moreover, Balashov and Zvolinskii[33] have studied the theoretical stresses and velocity fields, which occur during the displacement of a cone at a constant velocity in a rigid-plastic medium. In their study where plastic effects are predominant compared to viscous and inertial effects, they shown that the drag force depends on the yield stiffness of the medium and on the geometrical properties of the cone.

In geotechnics, the resistance of circular anchors dragged in clay media has been analyzed by Khatri and Kumar.[34] This numerical analysis reveals that the resistance factor increases with the penetration height of the anchor up to a critical height above which it remains constant. Nevertheless, the resistance factor is less modified by the anchor surface properties. Moreover, the penetration of the anchor in the rigid-plastic medium has led to the development of a plastic zone of which size increases with the penetration height.

Jossic and Magnin[10] have measured the drag coefficient of an adhesive conical obstacle with an apex angle of 90°

slowly moved in a shear thinning yield stress fluid. For Oldroyd numbers varying between 1 and 10, they obtained a drag coefficient of 9.9 and a stability criterion of 0.027; the stability criterion representing the critical value of the ratio between plasticity and gravity effects for which the cone is held in suspension.

Jossic et al.[29] have recently studied the flow of a shear thinning yield stress fluid perpendicular to an adhesive disc, that is, a cone of apex angle equal to 180°. They focused on the influence of the velocity on the drag coefficient and on the velocity fields and profiles. They obtained a drag coefficient of 9.2 and a stability criterion of 0.11.

The first part of this analysis focuses on the drag coefficients measurements. These measurements have been performed for different velocities and different cones whose characteristics are given in Table 1. Then, the second part pinpoints the kinematic fields obtained by particle image velocimetry (PIV). From these kinematic data, the shape and the extent of the rigid zones in the vicinity of the obstacles have been quantified. In this part, a particular attention has been paid on the sheared zone which occurs during the flow along the lateral surface of the cones. Finally, the contributions of the force on the lateral surface and on the cross section have been quantified from the kinematic measurements.

Theory

Piau[35] highlighted the elastoviscoplastic behavior of Carbopol 940. This behavior can be modelled by the Herschel–Bulkley model completed by the Hooke's model.[20–22,29] The first model is defined by the yield stress τ_0, the consistency K and the shear thinning index n. The latter model which is used below the yield stress τ_0 is defined by the shear elasticity modulus G. As the Hooke's model is valid only for small strains, the neo-Hookean model[36,37] is more likely to better describe the Carbopol behavior below the yield stress.

Based on this constitutive model, the expressions of the Reynolds and Oldroyd numbers[25,26] are:

$$\begin{cases} \mathrm{Re} = \dfrac{\rho {U_0}^{2-n} d^n}{K} & (1) \\ Od = \dfrac{\tau_0}{K\left(\frac{U_0}{d}\right)^n} & (2) \end{cases}$$

where ρ, d and U_0 respectively represent the fluid density, the cone's diameter and the displacement velocity. The quantities defining the cone's geometry and the flow configuration are given in Figure 1.

The characteristic time scale of the experiments can be evaluated by: $t_e \approx d/U_0$. Based on the evolution of the gel relaxation time, t_r, given in Ref. 20, the Weissenberg number can be estimated as follows:

Table 1. Geometrical Properties of the Cones

θ (°)	d (mm)	h (mm)	a (mm)	A (mm^2)
20	10	28.36	28.79	78.54
35	10	16.54	17.34	78.54
45	20	24.14	26.13	314.16
60	20	17.32	20	314.16
90	10	5	7.1	78.54
90	20	10	14.14	314.16
120	20	5.77	11.54	314.16
180	20	2	10	314.16

$$We = t_r/t_e \approx 0.56\left(\frac{U_0}{d}\right)^{0.38} \quad (3)$$

In this study, Eq. 3 provides Weissenberg numbers varying from 10^{-2} to 10^{-1}.

Moreover, as explained in Ref. 9, the plastic drag coefficient, C_d^*, defined in Ref. 10 can be modelled as follows:

$$C_d^* = \frac{F_d}{\tau_0 . A} = C_{d,\infty}^* + \frac{\beta}{Od^m} \quad (4)$$

where F_d is the drag force, $A = \frac{\pi d^2}{4}$ is the cross section of the cone, $C_{d,\infty}^*$ and $\frac{\beta}{Od^m}$ respectively represent the asymptotic drag coefficient, that is the plastic contribution and the viscous contribution to the drag coefficient.

The stability criterion, Y_{crit}, corresponding to the value of the ratio between plasticity and gravity effects, Y, for $Od \to \infty$ can then be defined in the case of the cone as follows:

$$Y_{crit} = \left(\frac{\tau_0}{gh\Delta\rho}\right)_{crit} = \frac{1}{3C_{d,\infty}^*} \quad (5)$$

where h is the height of the cone (Figure 1), g is the gravity and $\Delta\rho$ is the difference between the fluid and the cone densities.

Experimental Setup

The experimental setup and its technical details are given in Refs. 20 and 29. This setup enables both the measurements of the drag force and the visualization of the velocity fields around the cones whose geometrical properties are recapped in Table 1. The flow morphology considered here is depicted in Figure 1. In this figure, the flow field in the upstream of the cone is uniform and the fluid flows along the axis of symmetry of the cone. The flow velocity U_0 is kept constant. Its values are chosen about the μm/s to neglect inertial effects compared to viscous and plastic effects. The reference (O, x, y) is used to define the shape and the extent of the rigid and sheared zones around the cones. Its origin O corresponds to the middle of the apothem. The quantities δ and δ_0 along the y axis respectively represent the thicknesses of the sheared zone and of

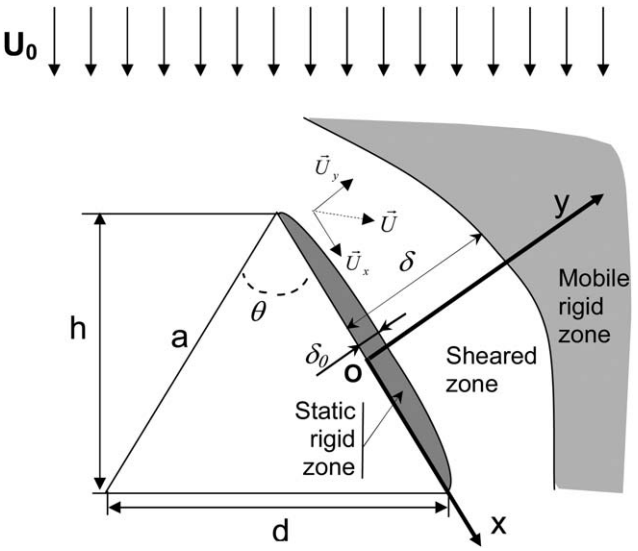

Figure 1. Flow configuration and notations.

the rigid static zone around the cone. Their evolutions as a function of the cone apex angle are given in the velocity field and profiles section.

To measure the drag forces, the cones have been linked by a nylon thread to a force sensor: a weighing balance, namely the PRECISA 1000C 3000D with a precision of 0.1 g. The diameter of the nylon thread is chosen equal to 0.4 mm to avoid the effects of the thread on the measurements. The sensor provides the temporal evolution of the mass during the flow. Then, the drag force undergone by the cone is obtained by subtracting the buoyancy forces from the constant force obtained in the steady state.

The tank containing the cone is moved at controlled velocities ranging from 1 to 200 μm/s, which are provided by a microcontrol plate controlled by an ITL09 unit. This tank is a square base parallelepiped with 200 mm sides and 300 mm height to neglect sides' effects. For visualizing the flow, the fluid has been seeded with reflective particles whose size varies between 5 and 30 μm and whose density is around 6.5×10^{-5}. The fluid was illuminated by a continuous laser, namely Spectra Physics, with a wavelength of 532 nm and a power of 2 W. The images obtained with a SONY CCD IRIS movie camera with a 55 mm lens are then analyzed with the PIV software Flow Manager V4.71. To hold the cones at a fixed position during the velocity fields' visualizations, all the cones except from the one with an apex angle of 180° have been stuck to a rigid disc of which diameter $d = 20$ mm. This disc is linked by mean of a screw to a vertical rigid rod with circular cross section. This leads to a "L"-shaped structure which is fixed in the Carbopol gel. Both the disc and the rod have a small thickness compared to the height of the cones so that they have little influence on the upstream flow.

Material and Rheometry

Piau[35] and Dimitriou et al.[38] give a critical and complete view of the data concerning Carbopol gel. This gel is widely used as a model of yield stress fluid for its transparency, its good stability over time and its viscoplastic behavior. It is also considered as non-thixotropic.[20,35,38–43] However, this non-thixotropic behavior remains controversial.[44] The microscopic structure of Carbopol gel is made of a suspension of deformable microgels swollen with a solvent. Piau[35] and Gutowski et al.[45] estimate the microgels' size to be between 2 and 20 μm. The yield stress of Carbopol gel is due to the spatial packing of the microgels. To avoid any slip at the wall of the cones, the cones were covered with a sandpaper whose roughness about 200 μm is higher than the characteristic size of Carbopol microgels.

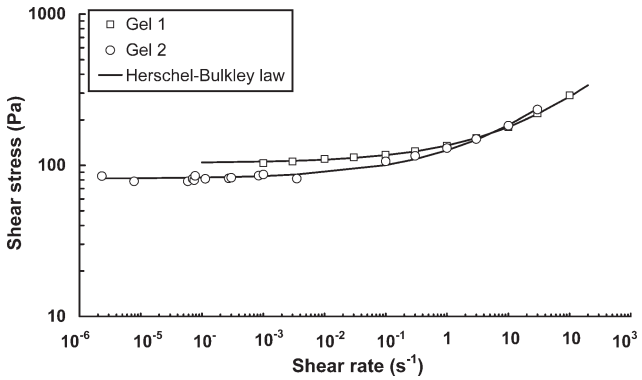

Figure 2. Flow curves of the gels.

Table 2. Rheological Properties of the Gels

	Gel 1	Gel 2
n	0.38	0.37
τ_0 (Pa)	103.6	81.5
K (Pas^n)	31.4	44

Two samples of Carbopol gels called "Gel 1" and "Gel 2" were used in this study. These samples were obtained by diluting Carbopol in distilled water. Then, the translucent acidic solutions obtained were neutralized by the addition of a 1 mol/l NaOH. This addition leads to a transparent gel with a pH of approximately 7 and a density of approximately 1000 kg/m^3. The rheological properties of the two gels were obtained by simple shear measurements at controlled speed with an ARES rheometer manufactured by TA Instruments. These measurements were performed at controlled temperature and controlled evaporation in a cone and plane cell for shear rates ranging from 10^{-6} to 100 s^{-1}. The cone used has an angle of 0.08 rad and a diameter of 49 mm. Its surface and the surface of the plane cell were covered with sandpaper with a roughness of approximately 200 μm to avoid slip.[42,43] The flow curves of Gels 1 and 2 obtained at $T = 23$°C are given in Figure 2. The parameters of the Herschel–Bulkley model determined by the least-squares method are given in Table 2. The uncertainties on the measured shear stresses are about 10%.

Results and Discussions

Drag coefficient and stability criterion

Figure 3 represents the evolution of the drag coefficient as a function of the Oldroyd number for different values of cone apex angles θ. The Oldroyd numbers range from 19 to 143, which correspond to flow velocities ranging from 1 to 150 μm/s. The parameters β, m and the asymptotic drag coefficient $C^*_{d,\infty}$ of Eq. 4 are recapped in Table 3.

For a given cone, the drag coefficient slowly decreases with the Oldroyd number before tending toward the asymptotic drag coefficient $C^*_{d,\infty}$ for Oldroyd numbers higher than 50. This implies for these Oldroyd numbers that the drag

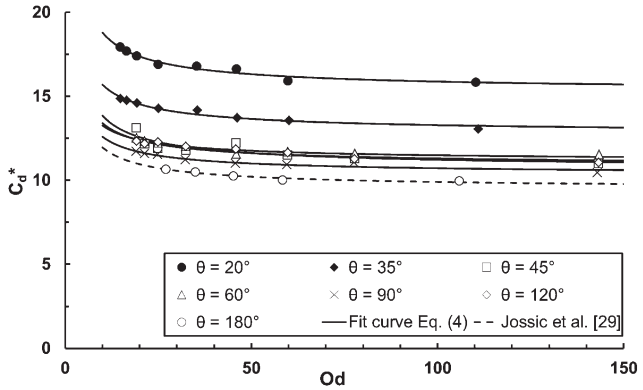

Figure 3. Evolutions of the drag coefficient as a function of Od for different values of θ (the evolution provided for $\theta = 90°$ is for the cone with $d = 20$ mm).

Table 3. Values of β, m, $C^*_{d,\infty}$ and Y_{crit} as a Function of θ

θ (°)	β	m	$C^*_{d,\infty}$	Y_{crit}
20	19		15.2	0.022
30	15.7		12.7	0.026
45	17.1		10.6	0.031
60	11.6	0.72	11.1	0.030
90	12.3		10.3	0.032
120	13.8		10.8	0.031
180	13.5		9.4	0.035

force undergone by the cone is no longer governed by the flow velocity but is directly proportional to the yield stress and the cross section of the cone.

For a given Oldroyd number, Figure 3 highlights an increase of the drag coefficient when the cone apex angle decreases. To understand the influence of the cone apex angle θ on the drag coefficient, Figure 4 represents the evolution of the asymptotic drag coefficient $C^*_{d,\infty}$ as a function of θ. Considering at first the cones with a diameter equal to 20 mm, the asymptotic drag coefficient for θ values higher than 90° remains constant despite a decrease in the lateral surface when θ increases. Therefore, it follows that the drag force does not depend on the cone apex angle, i.e. on the lateral surface but mainly depends on the yield stress and on the cross section.

Considering now the cones with a diameter equal to 10 mm, the drag coefficient for θ values lower than 90° increases when the cone apex angle decreases, i.e. when the lateral surface becomes more and more important in comparison with the cross section. In this range of cone apex angle, the influence of the lateral surface on the drag force becomes more and more important. This observation is in agreement with the evolution of the ratio between the lateral surface and the cross section which evolves as $1/\sin(\theta/2)$.

The experimental values of $C^*_{d,\infty}$ provided by Eq. 4 can be fitted by the following function which is not only straightforward but also consistent from a physical point of view:

$$C^*_{d,\infty} = 9.5 + \cot(\theta/2) \tag{6}$$

The first term of Eq. 6 which represents the contribution of the cross section is the plastic drag coefficient of a horizontal disc.[29] The second term, $\cot(\theta/2)$, represents the ratio between the drag forces on the lateral surface and the cross section. This term can simply be demonstrated by considering an elementary band of the cone located between z and $z + dz$ with a radius $r = z\tan(\theta/2)$, a length of $2\pi r$ and a width of $\frac{dz}{\cos(\theta/2)}$. As a first approximation, the shear stress on the lateral surface of the cone can be considered uniform and equal to the yield stress τ_0. The elementary band undergoes an elementary lateral drag force defined as $dF_{dl} = \tau_0 \cos(\theta/2) dS$ with $dS = 2\pi r \frac{dz}{\cos(\theta/2)}$. Therefore, the resulting drag force undergone by the lateral surface of the cone is

$$F_{dl} = \int_0^h \tau_0 * 2\pi r dz = \tau_0 \pi h^2 \tan(\theta/2) = \tau_0 \frac{\pi d^2}{4} \cot(\theta/2) \tag{7}$$

This first theoretical approach corroborates the second term of Eq. 6 even if the assumption of a uniform shear stress at the wall of the cone is a straightforward approach as this stress may be not uniform. Therefore, Eq. 6 can be understood as the sum of the drag force undergone by a disc[29] and the drag force exerted on the lateral surface of the cone.

The drag coefficient corresponding to $\theta = 6.4°$ provided in Figure 4 stems from the measurements performed by Jossic and Magnin[10] for a vertical cylinder with a slenderness factor of 5. This angle has been determined by assimilating the cylinder to a cone whose equivalent angle is defined by the ratio between the cross section and the lateral surface of the vertical cylinder. This point matches well with the fit curve.

Figure 4 also provides the evolution of the bearing cone factor N_{ch} obtained by Koumoto and Houlsby[32] as a function of the cone apex angle. This evolution is similar to that of the asymptotic drag coefficient. Like the asymptotic drag coefficient, the bearing cone factor decreases with the cone apex angle before levelling off at a plateau. Furthermore, the values of $C^*_{d,\infty}$ and N_{ch} are of the same order of magnitude even though the values of $C^*_{d,\infty}$ are higher than those of N_{ch}. This difference can be attributed to the fact that the cones used by Koumoto and Houlsby are not completely embedded in the considered medium. Therefore, the pressure force exerted on the cross section, i.e. the force due to the rear flow is not considered in the total force calculation.

The stability criterion Y_{crit} can be calculated from Eq. 5. The values of this quantity which vary between 0.02 and 0.04 (Table 3), are of the same order of magnitude as the value of 0.027 obtained by Jossic and Magnin[10] for a rough cone with $\theta = 90°$.

Since measuring the yield stress of complex fluids can be challenging, these drag coefficients measurements may constitute the basis for an alternative method for yield stress measurement. To that extent, whatever cone of this study could be used to determine at first the drag force corresponding to a very low velocity. Then, as the evolution of the asymptotic drag coefficient is provided as a function of the cone apex angle (Figure 4), an estimate of the yield stress value can be obtained by dividing the measured drag force by the asymptotic drag coefficient and the cross section of the cone. Once this value is known, the corresponding Oldroyd number has to be determined to check that it is high enough to consider the asymptotic drag coefficient. If not, three measurements have to be performed at three different velocities in order to compute τ_0, K and n from Eq. 4.

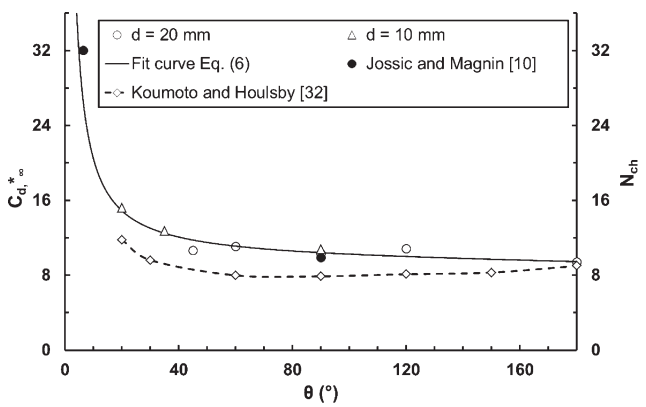

Figure 4. Evolutions of the asymptotic plastic drag coefficient (white triangles, black and white circles) and of the cone bearing factor (white diamonds) as a function of θ.

Velocity fields and profiles

This section focuses on the velocity field and profiles in the vicinity of the cones. This kinematic study was performed with Gel 2 and cones with 20 mm of diameter. The apothem of each cone will serve as length scale and the tank velocity U_0 as velocity scale.

Velocity Fields and Recirculation. Figure 5 provides the fields of the non-dimensional velocity U^* around each cone for $Od = 11$, i.e. at $U_0 = 150$ μm/s. In this figure, the cross section that appears at the bottom of each cone corresponds to the disc used to hold the cone at a fixed position. Figure 5 enables to analyze the influence of the cone apex angle θ on the flow morphology. The observed velocities fields are broadly similar. Far upstream, the flow velocity is constant and equal to the tank velocity U_0. This velocity slowly decreases toward 0 at the surface of the cone. This leads to the development of a zone of very low velocities in the immediate vicinity of the cone's edge.

In the plane (x, y) in Figure 1, the velocities progressively increase from the edge of the cone to reach the tank velocity U_0 far from it. The region where the flow velocity is equal to the tank velocity corresponds to the mobile rigid zone. The region between the cone and the mobile rigid zone is called the sheared zone. In the plane (x, y), the observed velocities in the immediate vicinity of the cone's edge become higher when the angle θ gets lower. Therefore, it follows that the thickness of the zone of low velocities increases when the cone apex angle θ increases. What is more, as θ increases, this zone entirely covers the cone's edge and tends toward a dome for $\theta = 180°$ as observed for the disc.[29]

The downstream flow reveals a conical zone with low velocities similar to that observed in the case of the disc.[29] In the wake of the cone, the velocities progressively increase and reach the tank velocity far from the cone.

It is worthwhile noting that a change of frame from the fixed frame attached to the cone to a fixed frame attached to the tank has highlighted the phenomenon of recirculation in the wake of the cones as it has been observed for the sphere,[18,20] the cylinder[22] and the disc.[29]

Influence of the Oldroyd Number. This paragraph analyzes the influence of the Oldroyd number on the velocity profiles along the y axis for $\theta = 90°$. Figure 6 represents the profiles of the non-dimensional velocity U^* along the y axis at $x^* = 0$ for $Od = 11$ and $Od = 72$, i.e. at $U_0 = 150$ μm/s and $U_0 = 1$ μm/s, respectively. The experimental data can be fitted by the following equation

$$U^* = \frac{1 + k_1 e^{-k_2 y^*}}{1 + k_3 e^{-k_4 y^*}} \tag{8}$$

where $y^* = \frac{y}{a}$, k_1, k_2, k_3 and k_4 are parameters determined by the least-squares method. The values of k_1, k_2, k_3, and k_4 are given in Table 4.

In Figure 6, the profile corresponding to $Od = 72$ is more disturbed by noise effects due to the large time intervals between the successive images for this flow velocity. Nevertheless, both profiles show similar evolutions starting by a low velocity region in the vicinity of the lateral surface beyond which the velocities progressively increase up to the tank velocity U_0 far from the cone's edge. The thickness of the sheared zone δ can be evaluated from Figure 6. To this end, the criterion chosen is $U^* = 99\%$. Applying this criterion on Eq. 8 provides the non-dimensional thickness of the sheared zone δ^*, which is estimated at 1.3 for $Od = 11$ and at 0.9 for $Od = 72$. The difference between these two values of δ^* is about 44%. With regards to the noise previously evoked which leads to higher experimental uncertainties for $Od = 72$, it results that the flow morphology is only slightly influenced by the Oldroyd number in the range of Oldroyd numbers considered here. The two velocity profiles are very similar except in a very small interval, for y^* ranging from

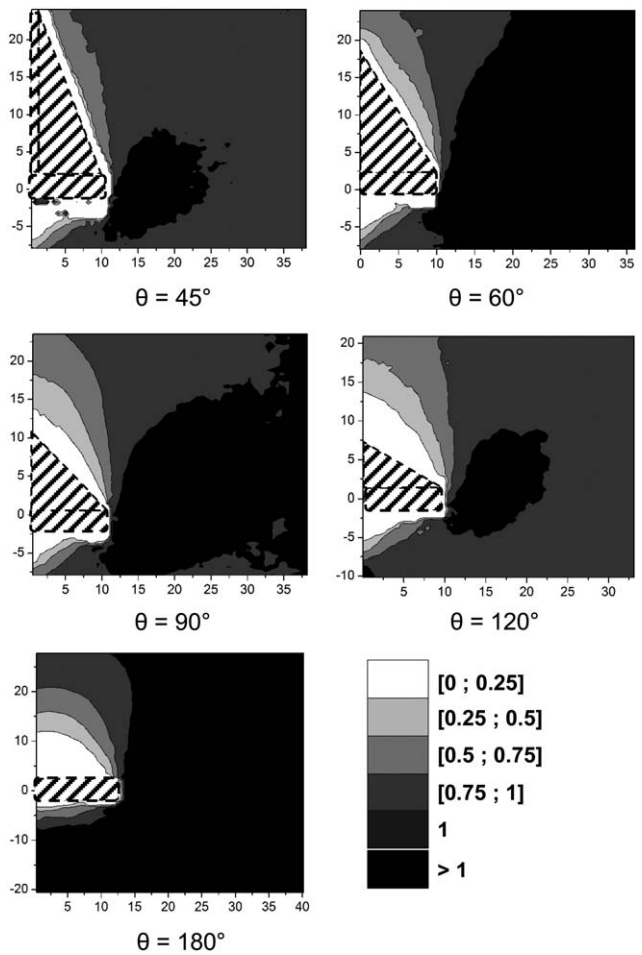

Figure 5. Fields of the non-dimensional velocity U^* for $Od = 11$ (the cone is represented by the shaded area).

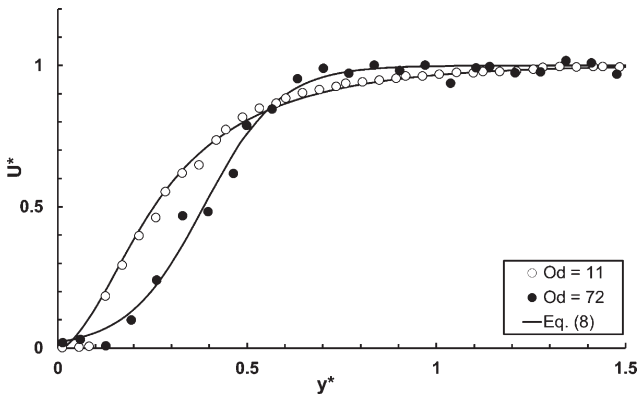

Figure 6. Profiles of the non-dimensional velocity U^* located at $x^* = 0$ for $\theta = 90°$ as a function of Od.

Table 4. Theoretical Velocity Profiles Properties as a Function of θ

θ (°)	Od	k_1	k_2	k_3	k_4
45	11	−1.03	5.08	−0.73	6.68
60	11	−1.05	5.61	0.25	5.12
90	11	−1.06	3.44	2.5	12.07
90	72	0	8	46.67	10
120	11	−1.1	1.80	2.92	4.42
180	11	−1.17	0.75	8.78	3.12

0.1 to 0.5. This result corroborates the one observed for the disc.[29] For this asymptotic case, $\theta = 180°$, no significant influence of the Oldroyd number on the shape and the size of the rigid and sheared zones has been observed.

Influence of the Cone Apex Angle. This section focuses on the influence of the geometry of the cone on the velocity fields and profiles in the plane (x, y). This influence is analyzed at $Od = 11$.

Figure 7 represents the profiles of the non-dimensional velocity U^* along the y axis at $x^* = 0$ for different values of θ for $Od = 11$. The experimental data can be fitted by Eq. 8 with parameters given in Table 4. Figure 7 which reveals broadly similar velocity profiles corroborates the differences previously evoked concerning the close vicinity of the edge of each cone. The velocity profiles obtained for $\theta = 45°$, $\theta = 60°$, and $\theta = 90°$ rise immediately, whereas the two other profiles spread on the zone of low velocities. Moreover, Figure 7 shows that the thickness of the sheared zone δ increases with the angle θ. To thoroughly analyze the sheared zone developing around the cone, the evolution of δ^* as a function of θ is given in Figure 8. These values of δ^* have been obtained with the criterion $U^* = 99\%$ applied in Eq. 8. This figure reveals that the thickness of the sheared zone levels off at a value of 0.8 for θ lower than 45°. Above this value it increases with the angle θ. The evolution of δ^* can be fitted by the following equation whose parameters λ_1, λ_2, and λ_3 are recapped in Table 5

$$\delta^* = \lambda_1 \theta^{\lambda_2} + \lambda_3 \tag{9}$$

To go one step further in the analysis of the low velocities zones observed in Figures 5 and 7, Figure 9 provides the fields of the second invariant of the strain rates tensor D_{II} for each cone. In the plane (x, y), Figure 9 reveals two main features depending on the cone apex angle θ. For θ lower

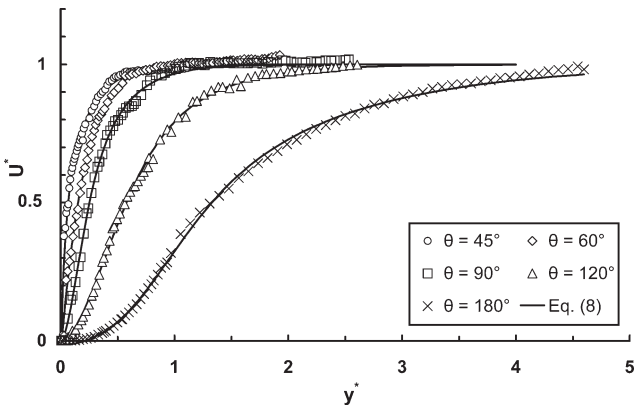

Figure 7. Profiles of the non-dimensional velocity U^* located at $x^* = 0$ for different values of θ for $Od = 11$.

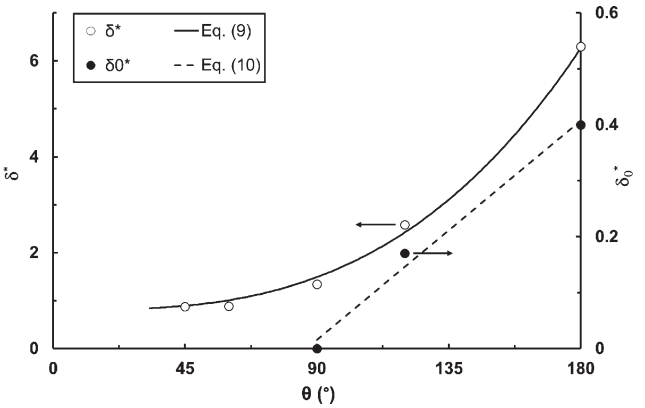

Figure 8. Evolutions of the non-dimensional thicknesses of the sheared zone and upstream static rigid zone as a function of θ for $Od = 11$.

than 90°, two main zones can be observed: a first zone representing the sheared zone where the second invariant starts with relatively high values in the vicinity of the cone before slowly tending toward almost zero values in a white zone which corresponds to the mobile rigid zone. For θ higher than 90°, the feature is almost similar except that another white zone appears in the immediate vicinity of the cone. This zone corresponds to the upstream static rigid zone whose thickness δ_0 seems to increase as θ increases. A rigid zone either static or mobile is normally described by zero values of the second invariant of the strain rates tensor. The computations of D_{II} are disturbed by the uncertainties of the velocities measurements and the values of D_{II} are then provided with an uncertainty about 20%. The criterion chosen here to first approximate the thickness δ_0 is that $D_{II} \geq 0.002$ s^{-1}. The evolution of the non-dimensional thickness δ_0^* obtained with this criterion as a function of the angle θ is given in Figure 8. This evolution can be fitted by the following equation whose parameters λ_4 and λ_5 are recapped in Table 5

$$\delta_0^* = \lambda_4 \theta + \lambda_5 \tag{10}$$

Since the velocities fields and profiles are known, the wall shear rates $\dot{\gamma}_w$ and the wall shear stresses τ_w can be estimated for each cone. The shear rates can at first be approximated by the variation of the tangential velocity U_x (Figure 1) along y in the vicinity of the wall. Then, the Herschel–Bulkley model applied in the case of a simple shear enables to estimate the wall shear stress. Figure 10 provides the evolutions of the wall shear rate $\dot{\gamma}_w$ and the resulting non-dimensional wall shear stress $\tau_w^* = \frac{\tau_w}{\tau_0}$ at $x^* = 0$ and $y^* = 0$ as a function of θ. The variations of $\dot{\gamma}_w$ can be fitted by the following equation:

Table 5. Values of Parameters of Eqs. 9 and 10

Parameters	Values	Conditions
λ_1	9.3×10^{-7}	–
λ_2	3	–
λ_3	0.8	–
λ_4	4.4×10^{-3}	$\theta > 90°$
λ_5	−0.38	$\theta > 90°$

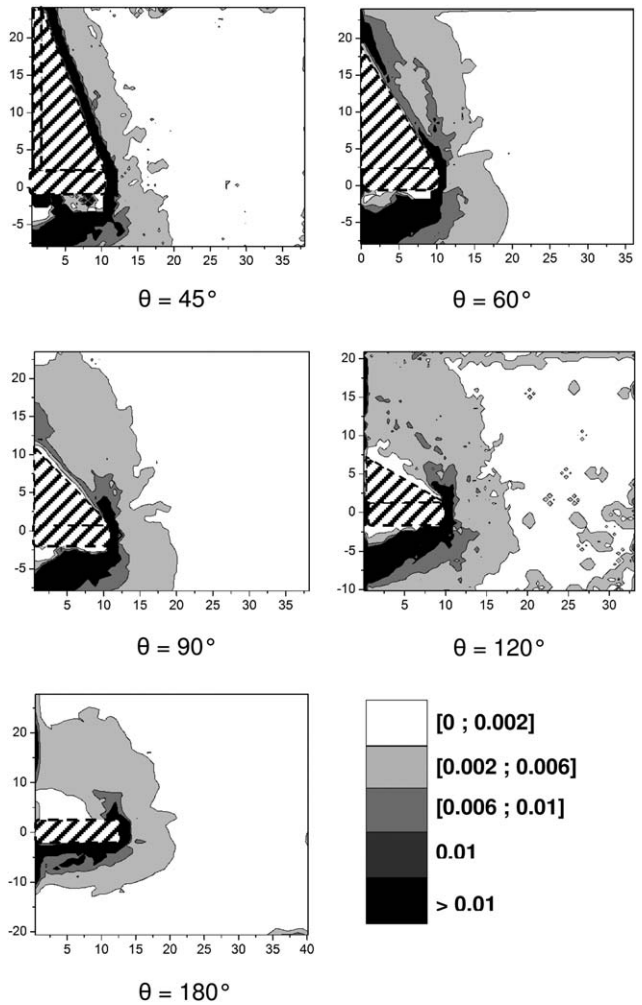

Figure 9. Fields of the second invariant of the strain rate tensor around the cones for *Od* = 11 (the cone is represented by the shaded area).

$$\dot{\gamma}_w = 2341 \cdot \theta^{-2.67} \tag{11}$$

Figure 10 reveals high values of $\dot{\gamma}_w$ for small cone apex angles which sharply decrease for θ lower than 90°. The shear rates observed for these angles are non-zero; a tendency which is consistent with the velocity fields (Figure 6) and the fields of the second invariant of the strain rates tensor (Figure 9) observed for θ lower than 90° which do not seem to show an upstream static rigid zone. Above 90°, the wall shear rate varies slightly with the angle θ and its values are lower than 0.01 s^{-1}. For $\theta = 120°$ and $\theta = 180°$, the values of $\dot{\gamma}_w$ are respectively of 0.006 and 0.002 s^{-1}. At a first estimation those values are close to the ones provided by Figure 9 for $\theta = 120°$ and $\theta = 180°$. Moreover, the decrease of $\dot{\gamma}_w$ is consistent with the increase of the extent of the low velocities zones with the cone apex angle θ. With regard to the relation between the shear rate and the shear stress, the same evolution is seen for the non-dimensional wall shear stress.

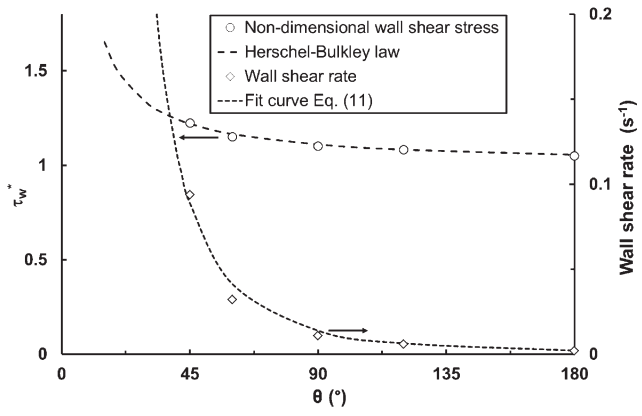

Figure 10. Evolutions of the wall shear rate and non-dimensional wall shear stress obtained at *x = 0 as a function of θ for *Od* = 11.**

Table 6. Values of $\dot{\gamma}_w$ as a Function of θ for Three Values of *x and for *Od* = 11**

*x**	$\theta = 45°$	$\theta = 60°$	$\theta = 90°$	$\theta = 120°$	$\theta = 180°$
−0.5	0.05	0.03	0.02	0.006	0
0	0.094	0.032	0.011	0.006	0.002
0.5	0.13	0.13	0.1	0.081	0.07

Concerning the influence of the position on the wall shear rates, Table 6 shows that the wall shear rates are quite analogous between the top of the cone and the origin O for θ higher than 60°. Nevertheless, the corresponding values are lower than the ones observed at $x^* = 0.5$ for θ higher than 60°. In fact, the flow is slowed at the top of the cone. Then the gel flows along the edge of the cone where the velocity is zero due to adherence conditions before being accelerated at the bottom of the cone due to the discontinuity in the geometry. For $\theta = 45°$, Table 6 shows a quite regular evolution of the wall shear rate.

Since the wall shear rates are estimated, the wall shear stresses can be determined according to the Herschel–Bulkley model. Then, the drag force exerted on the lateral surface can be calculated by integrating the wall shear stresses as explained in Eq. 7. If this equation relies on the assumption of a uniform wall shear stress, the wall shear rates given in Table 6 reveal that this assumption can no longer be used. However, since the wall shear rates do not vary a lot, a first estimation of the lateral drag force can be obtained by simply averaging the three values of wall shear stresses. Table 7 shows the resulting values for the ratio between the drag force exerted on the lateral surface and the drag force as a function of the cone apex angle. These values confirm the observations made in the drag coefficient and stability criterion section that the influence of the lateral section on the drag force is less marked for θ values higher than 90°. Table 7 also compares the drag forces exerted on the lateral surface resulting from PIV measurements and Eq. 7. The ratio between these forces is estimated at 1.2 for θ values lower than 90° and at 1.1 for θ values higher than 90°. These ratios reveal that both drag forces exerted on the lateral surface are

Table 7. Comparison of the Drag Force Exerted on the Lateral Surface to the Drag Force and to the Drag Force provided by Eq. 7 at *Od* = 11

θ (°)	F_{dl}/F_d	F_{dl}/F_{dl} (Eq. 7)
45	0.22	1.2
60	0.16	1.19
90	0.09	1.15
120	0.05	1.12
180	0	1.1

of the same order of magnitude. The slight difference between them can be attributed to the difference of Oldroyd numbers and the assumptions made for computing them.

Conclusion

This experimental study focuses on the creeping flow of a viscoplastic fluid around conical obstacles. The evolutions of the drag coefficient as a function of the Oldroyd number and the cone apex angle have been at first analyzed. For a given cone apex angle, the drag coefficient decreases with the Oldroyd number and tends toward an asymptotic value only governed by the yield stress. Furthermore, for a given Oldroyd number, it increases with the cone apex angle. Correlations have been proposed to model the evolutions of the drag coefficient as a function of the Oldroyd number and the cone apex angle. This analysis of drag coefficients may be a new good alternative for measuring the yield stress of complex fluids.

The flow morphology has also been analyzed through PIV measurements. The results obtained have enabled to quantify not only the velocity fields and profiles but also the thicknesses of both the upstream static rigid zone and the sheared zone in the plane (x, y). The influences of the Oldroyd number and of the cone apex angle have been finely analyzed. The thicknesses of both the upstream static rigid zone and the sheared zone increase with the cone apex angle. What is more, a fitting equation has been proposed to model the experimental velocity profiles. In addition, the wall shear stresses have been estimated from the PIV measurements. These estimations have enabled to quantify the contribution of the drag force exerted on the lateral surface to the drag force.

This analysis has been performed with a transparent and non-thixotropic yield stress fluid. To consolidate the current results, the experimental methodology could be used for other types of yield stress fluids not necessarily transparent for drag measurements.

Acknowledgments

The Laboratoire Rhéologie et Procédés is part of the LabEx Tec 21 (Investissements d'Avenir - Grant agreement n° ANR-11-LABX-0030). Mr. Albert Magnin thanks Mr. Nicolas Mougin from the Rheonis Company for his helpful discussions on the rheology of Carbopol gels.

Notation

a = apothem, m
A = cross section, m^2
d = diameter, m
D_{II} = second invariant of the strain rates tensor, s^{-1}
F_d = drag force, N
F_{dl} = drag force exerted on the lateral surface, N
g = gravity, m/s^2
G = shear elasticity modulus, Pa
h = height, m
K = consistency, Pas^n
m = index-
n = shear thinning index
t_e = characteristic time scale of the experiment, s
t_r = relaxation time, s
U = norm of the velocity, m/s
U_0 = tank velocity, m/s
U_x = tangential velocity, m/s
U_y = normal velocity, m/s
x = tangential unitary vector, m
y = normal unitary vector, m

Greek letters

β = parameter
δ = thickness of the sheared zone, m
δ_0 = thickness of the upstream static rigid zone, m
$\dot{\gamma}_w$ = wall shear rate, s^{-1}
θ = apex angle, °
ρ = density, kg/m^3
$\Delta\rho$ = difference between fluid density and cones density, kg/m^3
τ_w = wall shear stress, Pa
τ_0 = yield stress, Pa

Non-dimensional numbers

C_d^* = drag coefficient
$C_{d,\infty}^*$ = asymptotic drag coefficient
δ^* = non-dimensional thickness of the sheared zone corresponding to δ/a
δ_0^* = non-dimensional thickness of the upstream static rigid zone corresponding to δ_0/a
Od = Oldroyd number
Re = Reynolds number
U^* = non-dimensional velocity corresponding to U^*/U_0.
x^* = non-dimensional tangential unitary vector corresponding to x/a.
y^* = non-dimensional normal unitary vector corresponding to y/a.
Y_{crit} = stability criterion

Literature Cited

1. Andres UT. Equilibrium and motion of spheres in a viscoplastic liquid. *Sov. Phys. Doklady (USA)*, 1961;5:723–725.
2. Chhabra RP. *Bubbles, Drops and Particles in Non-Newtonian Fluids, 2nd ed,* Boca Raton: CRC Press, 2006.
3. Beris AN, Tsamopoulos JA, Armstrong RC, Brown RA. Creeping motion of a sphere through a Bingham plastic. *J Fluid Mech.* 1985; 158:219–244.
4. Atapattu DD, Chhabra RP, Uhlherr PHT. Wall effect for spheres falling at small Reynolds number in a viscoplastic medium. *J Non-Newtonian Fluid Mech.* 1990;38(1):31–42.
5. Atapattu DD, Chhabra RP, Uhlherr PHT. Creeping sphere motion in Herschel-Bulkley fluids: flow field and drag. *J Non-Newtonian Fluid Mech.* 1995;59:245–265.
6. Beaulne M, Mitsoulis E. Creeping motion of a sphere in tubes filled with Herschel-Bulkley fluids. *J Non-Newtonian Fluid Mech.* 1997; 72:55–71.
7. Blackery J, Mitsoulis E. Creeping motion of a sphere in tubes filled with a Bingham plastic material. *J Non-Newtonian Fluid Mech.* 1997;70:59–77.
8. Hariharaputhiran M, Subramanian RS, Campbell GA, Chhabra RP, The settling of spheres in a viscoplastic fluid. *J Non-Newtonian Fluid Mech.* 1998;79:87–97.
9. Merkak O, Jossic L, Magnin A. Spheres and interactions between spheres moving at very low velocities in a yield stress fluid. *J Non-Newtonian Fluid Mech.* 2006;133(2–3):99–108.
10. Jossic L, Magnin A. Drag and stability of objects in a yield stress fluid. *AIChE J.* 2001;47(12):2666–2672.
11. Liu BT, Muller SJ, Denn MM. Convergence of a regularization method for creeping flow of a Bingham material about a rigid sphere. *J Non-Newtonian Fluid Mech.* 2002;112:179–191.
12. Liu BT, Muller SJ, Denn MM. Interactions of two rigid spheres translating collinearly in creeping flow in a Bingham material. *J Non-Newtonian Fluid Mech.* 2003;113:49–67.
13. Briscoe BJ, Glaese M, Luckham PF, Ren S. The falling of spheres through Bingham fluids. *Colloids Surf.* 1992;65:69–75.
14. Dolejš V, Doleček P, Šiška P. Drag and fall of a spherical particle in generalized Newtonian and viscoplastic fluids. *Chem Eng Process.* 1998;37:189–195.
15. He YB, Laskowski JS, Klein B. Particle movement in non-Newtonian slurries: the effect of yield stress on dense medium separation. *Chem Eng Sci.* 2001;56(9):2991–2998.
16. Yu Z, Wachs A. A fictitious domain method for dynamic simulation of particle sedimentation in Bingham fluids. *J Non-Newtonian Fluid Mech.* 2007;145(2–3):78–91.
17. Tabuteau H, Coussot P, de Bruyn JR. Drag force on a sphere in steady motion through a yield stress fluid. *J Rheol.* 2007;51(1):125–137.

18. Putz AMV, Burghelea TI, Frigaard IA, Martinez DM. Settling of an isolated spherical particle in a yield stress shear thinning fluid. *Phys. Fluids*. 2008;20(3):1–11.
19. Deglo De Besses B, Magnin A, Jay P. Sphere drag in a viscoplastic fluid. *AIChE J*. 2004;50(10):2627–2629.
20. Ahonguio F, Jossic L, Magnin A. Influence of surface properties on the flow of a yield stress fluid around spheres. *J Non-Newtonian Fluid Mech*. 2014;206:57–70.
21. Jossic L, Magnin A. Drag of an isolated cylinder and interactions between two cylinders in yield stress fluids. *J Non-Newtonian Fluid Mech*. 2009;164:9–16.
22. Tokpavi DL, Jay P, Magnin A, Jossic L. Experimental study of the very slow flow of a yield stress fluid around a circular cylinder. *J Non-Newtonian Fluid Mech*. 2009;164:35–44.
23. Mossaz S, Jay P, Magnin A. Experimental study of stationary flows of a yield stress fluid around cylinder. *J Non-Newtonian Fluid Mech*. 2012;189–190:40–52.
24. Nirmalkar N, Chhabra RP, Poole RJ. On creeping flow of a Bingham plastic fluid past a square cylinder. *J Non-Newtonian Fluid Mech*. 2012;171–172:17–30.
25. Oldroyd JG. Two-dimensional plastic flow for a Bingham fluid. A boundary-layer theory for slow motion. *Proc. Camb. Philos. Soc*. 1947;43:383–395.
26. Oldroyd JG. A rational formulation of the equations of plastic flow for a Bingham fluid. *Proc. Camb. Philos. Soc*. 1947;43:100–105.
27. Piau JM. Viscoplastic boundary layer. *J Non-Newtonian Fluid Mech*. 2002;102:193–218.
28. Piau JM, Debiane K. The adhesive or slippery flat plate viscoplastic boundary layer for a shear-thinning power-law viscosity. *J Non-Newtonian Fluid Mech*. 2004;117(2–3):97–107.
29. Jossic L, Ahonguio F, Magnin A. Flow of a yield stress fluid perpendicular to a disc. *J Non-Newtonian Fluid Mech*. 2013;191:14–24.
30. Houlsby GT. Theoretical analysis of the fall cone test. *Geotechnique*. 1982;32(2):111–118.
31. Houlsby GT, Wroth CP. Calculation of stresses on shallow penetrometers and footings. In: *Proceedings of the International Union of Theoretical and Applied Mechanics (IUTAM) / International Union of Geodesy and Geophysics (IUGG) Symposium on seabed Mechanics*. Newcastle upon Tyne, September 1993;107–112.
32. Koumoto T, Houlsby GT. Theory and practice of the fall cone test. *Geotechnique*. 2001;51(8):701–712.
33. Balashov DB, Zvolinskii NV. Flow of a rigid-plastic medium around a cone. *Mech Solids*. 1996;31(3):39–45.
34. Khatri VN, Kumar J. Vertical uplift resistance of circular plate anchors in clays under undrained condition. *Comput Geotech*. 2009; 36:1352–1359.
35. Piau JM. Carbopol gels: elastoviscoplastic and slippery glasses made of individual swollen sponges. Meso- and macroscopic properties, constitutive equations and scaling laws. *J Non-Newtonian Fluid Mech*. 2007;144:1–29.
36. Höhler R, Cohen-Addad S, Labiausse V. Constitutive equation to describe the nonlinear elastic response of aqueous foams and concentrated emulsions. *J Rheol*. 2004;48:679–690.
37. Labiausse V, Höhler R, Cohen-Addad S. Shear induced normal stress differences in aqueous foams. *J Rheol*. 2007;51:479–492.
38. Dimitriou CJ, Ewoldt RH, McKinley GH. Describing and prescribing the constitutive response of yield stress fluids using large amplitude oscillatory shear stress (LAOStress). *J Rheol*. 2013;57(1):27–70.
39. BF Goodrich Literature, Cleveland, 1997.
40. Møller PCF, Fall A, Bonn D. Origin of apparent viscosity in yield stress fluids below yielding. *Euro Phys Lett*. 2009;87(38004):1–6.
41. Møller PCF, Mewis J, Bonn D. Yield stress and thixotropy: On the difficulty of measuring yield stresses in practice. *Soft Matter*. 2006; 2:274–283.
42. Magnin A, Piau JM. Cone and plate rheometry of yield stress fluids. Study of an aqueous gel. *J Non-Newtonian Fluid Mech*. 1990;36:85–108.
43. Magnin A, Piau JM. Shear rheometry of fluids with a yield stress. *J Non-Newtonian Fluid Mech*. 1987;23:91–106.
44. Putz AMV, Burghelea TI. The solid-fluid transition in a yield stress shear thinning physical gel. *Rheol Acta*. 2009;48:673–689.
45. Gutowski IA, Lee D, de Bruyn JR, Frisken BJ. Scaling and mesostructure of Carbopol dispersions. *Rheol Acta*. 2012;51(5):441–450.

Manuscript received May 28, 2014, and revision received Sep. 9, 2014.